HHS Public Access
Author manuscript
ACS Nano. Author manuscript; available in PMC 2021 April 28.

Published in final edited form as:
ACS Nano. 2020 April 28; 14(4): 4255–4264. doi:10.1021/acsnano.9b09618.

Osteotropic Radiolabeled Nanophotosensitizer for Imaging and Treating Multiple Myeloma

Rui Tang[1,‡], **Alexander Zheleznyak**[1,‡], **Matthew Mixdorf**[1], **Anchal Ghai**[1], **Julie Prior**[1], **Kvar C. L. Black**[1], **Monica Shokeen**[1,2], **Nathan Reed**[3], **Pratim Biswas**[3], **Samuel Achilefu**[1,2,4,*]

[1]Department of Radiology, Washington University School of Medicine, St. Louis, MO, 63110, USA

[2]Department of Biomedical Engineering, Washington University in St. Louis, St. Louis, MO, 63105, USA

[3]Department of Energy, Environmental and Chemical Engineering, Washington University in St. Louis, St. Louis, MO, 63112, USA

[4]Departments of Medicine and Biochemistry & Molecular Biophysics, Washington University School of Medicine, St. Louis, MO, 63110, USA

Abstract

Rapid liver and spleen opsonization of systemically administered nanoparticles (NPs) for *in vivo* applications remains the Achilles' heel of nanomedicine, allowing only a small fraction of the materials to reach the intended target tissue. Although focusing on diseases that reside in the natural disposal organs for nanoparticles is a viable option, it limits the plurality of lesions that could benefit from nanomedical interventions. Here we designed a theranostic nanoplatform consisting of reactive oxygen (ROS)-generating titanium dioxide (TiO_2) NPs, coated with a tumor-targeting agent, transferrin (Tf), and radiolabeled with a radionuclide (^{89}Zr) for targeting bone marrow, imaging the distribution of the NPs, and stimulating ROS generation for cell killing. Radiolabeling of TiO_2 NPs with ^{89}Zr afforded thermodynamically and kinetically stable chelate-free ^{89}Zr-TiO_2-Tf NPs without altering the NP morphology. Treatment of multiple myeloma (MM) cells, a disease of plasma cells originating in the bone marrow, with ^{89}Zr-TiO_2-Tf generated cytotoxic ROS to induce cancer cell killing *via* apoptosis pathway. Positron emission tomography/X-ray computed tomography (PET/CT) imaging and tissue biodistribution studies revealed that *in vivo* administration of ^{89}Zr-TiO_2-Tf in mice leveraged the osteotropic effect of ^{89}Zr to selectively localize about 70% of the injected radioactivity in mouse bone tissue. A combination of small animal PET/CT imaging of NP distribution and bioluminescence imaging of cancer progression showed that a single dose ^{89}Zr-TiO_2-Tf treatment in a disseminated MM mouse model completely inhibited cancer growth at euthanasia of untreated mice and at least doubled the survival of treated mice. Treatment of the mice with cold Zr-TiO_2-Tf, ^{89}Zr-oxalate, or

[*]**Corresponding Author**: Samuel Achilefu, Campus Box 8225, 4515 McKinley Ave, St. Louis, MO 63110. Tel: 1-314-362-8599 Fax: 1-314-362-8599, achilefu@wustl.edu.
[‡]These authors contributed equally to this work.
Author Contributions
All authors contributed to writing the manuscript and have given approval to the final version of the manuscript.

COMPETING INTERESTS
The authors have declared that no competing interest exists.

^{89}Zr-Tf had no therapeutic benefit compared to untreated controls. This study reveals an effective radionuclide sensitizing nanophototherapy paradigm for the treatment of MM and possibly other bone-associated malignancies.

Keywords

multiple myeloma; Zr-89; cancer; nanoparticles; Cerenkov radiation

The promise of nanomedicine in cancer therapy resides in the ability to deliver high payloads of drugs to cancer, amplify imaging signals,[1–5] optimize combination therapies, and improve theranostic strategies.[6–8] As vectors for drug delivery, nanoparticles (NPs) have the coveted advantages of modifying drug pharmacokinetics *in vivo*,[9–14] controlling drug release,[15–18] optimizing blood circulation half-lives,[9] improving biodistribution profiles,[19] increasing tissue permeability,[20–23] and enhancing metabolic stability of drugs.[24, 25] For imaging applications, some NPs exhibit intrinsic properties that facilitate their use as imaging agents.[26–30] Typical examples include light-emitting quantum dots for fluorescence imaging and ultra-small superparamagnetic iron oxide particles as magnetic resonance imaging (MRI) contrast agents.[31] Despite these benefits, clinical translation of most nanoparticle-based therapies and imaging agents has remained a challenge, in part due to the low percentage of injected dose that reaches the target tissues. This problem is particularly prevalent in metal-based nanoparticles that rapidly clear from circulation *via* liver, kidney, spleen or lung uptake. While some studies have leveraged this natural distribution pattern to deliver drugs and image the clearance organs, the lack of biological control limits the effectiveness and confines the disease type investigated. As a result, a large amount of disease-targeted NPs is needed to achieve a therapeutic effect, creating uneasiness about potential long-term toxicity.

Other than the aforementioned NP clearance organs, bone is an easily attainable tissue for targeted NP delivery. Coating nanoparticles with calcium-chelating ligands such as phosphonates is a viable option, but this does not alleviate the non-specific distribution in the liver and spleen. Previous studies have shown that some metals naturally home to the bone.[32] This feature is used effectively to design radiopharmaceuticals such as ^{89}Sr, ^{153}Sm, ^{186}Re, and ^{223}Ra for treating bone diseases and palliating pain.[33, 34] By providing localized radiation, these agents can selectively ablate proliferating osteoclasts induced by cancer cells. However, the high dose of radioactivity employed can have significant side effects and in most cases, relapse is a frequent occurrence. Instead of directly killing cells with energetic particles, low dose positron-emitting radionuclides could be used to sensitize the therapeutic effects of drugs in the bone.

We recently reported the use of low-dose radionuclides to potentiate the therapeutic effects of ROS-generating TiO_2 NPs.[35–37] We demonstrated that the approach is capable of inhibiting tumor growth with minimal side effects *via* sequential administration of the NPs first, followed by radionuclides. Among other mechanisms, we found that TiO_2 NPs can harvest the UV light from Cerenkov radiation of fluorine-18 fluorodeoxyglucose (^{18}FDG) to stimulate ROS generation. However, the uptake of ^{18}FDG in bone is only twice higher in disseminated tumor-bearing mice than in healthy mice. Recent studies have shown that some ^{89}Zr chelates can distribute to diverse organs in mice, including bone tissue.[38, 39] Although the selective osteotropism of ^{89}Zr oxalate was lost when chelated with desferrioxamine (DFO)[39] or adsorbed on liposomal membranes,[38] these suggest that integrating Zr into metal-based NPs could retain osteotropism if stabilized on an NP platform.

In this study, we developed a chelate-free ^{89}Zr-TiO_2 NPs, which were coated with a tumor-targeting Tf to afford thermodynamically and kinetically stable ^{89}Zr-TiO_2-Tf NPs. We then demonstrated the enhancement of ROS generation of the NPs compared to equivalent ^{89}Zr oxalate *in vitro*. The ^{89}Zr-TiO_2-Tf exhibited a high selectivity for bone, depositing about 70% of the injected radioactivity to the tissue. Administration of ^{89}Zr-TiO_2-Tf in disseminated MM mouse model, a bone-associated tumor, inhibited cancer growth and doubled the survival of the treated mice compared to the time of euthanasia of the untreated cohort. These results reveal an approach for bone-associated cancer therapy and uncover a potential strategy to treat bone lesions.

RESULTS AND DISCUSSION

Chelate-free Radiolabeling and Transferrin Coating of TiO_2 NPs

A major goal of this study is to deliver radiolabeled NPs to bone tissue with minimal uptake in the traditional NP clearance organs such as the lungs, liver, kidney, and spleen. Although Zr has been shown to possess osteotropic properties, the selectivity for bone depends on the nature of the metal. Chelation with DFO, for example, abrogates this feature.[39] As such, we sought a chelate-free approach to incorporate ^{89}Zr into TiO_2 NPs. Previous reports suggest that chelate-free, heat-induced ^{89}Zr radiolabeling of metal oxide NPs could be achieved through direct chemisorption.[40–44] We also explored the use of Tf to further stabilize the adsorbed Zr, enhance dispersion in aqueous medium, and target Tf receptor-expressing tumor cells. Apo-transferrin is known to chelate several metals such as Fe and Ti.[45, 46] The overexpression of Tf receptor on rapidly dividing cells is essential for recruiting Fe as a co-factor during DNA synthesis.[47] We recently demonstrated that TiO_2-coated Tf is capable of targeting HT1080 fibrosarcoma and A549 non-small cell lung carcinoma.[48] Postulating that a combination of Zr and Tf attachment to TiO_2 would retain the osteotropic properties of Zr and target cancer cells, we used a chelate-free, heat-induced method,[40] to directly label anatase TiO_2 NPs with ^{89}Zr and coated the radiolabeled ^{89}Zr-TiO_2 NPs with Tf (Scheme 1).

The ^{89}Zr radiolabeling of the TiO_2 NPs was confirmed by radio-TLC using 50 mM DTPA aqueous eluent at pH 7.5 (Figure 1A). The final radiochemical yield of purified ^{89}Zr-TiO_2-Tf was >95% with specific activity of 18.5 MBq/mg. We further explored the efficiency of ^{89}Zr labeling by varying the TiO_2 NP concentrations, while maintaining ^{89}Zr activity at 9.25 MBq. We found that the radiochemical yield was > 98%, resulting in a specific activity of approximately 18.5 MBq/mg when radiolabeling 0.5 mg of TiO_2 NPs (Figure 1B). At lower concentrations of TiO_2 NPs, the radiochemical yield dropped significantly. Therefore, 0.5 mg of TiO_2 and 9.25 MBq ^{89}Zr were used for the NP construct preparation and subsequent studies. Overall, the heat-induced radiolabeling provided efficient chemisorption of ^{89}Zr on the TiO_2 NP surfaces, with high radiochemical purity and yield. The direct association of $^{89}Zr^{4+}$ with oxygen atoms on the surface of the multi-oxygen containing TiO_2 NPs[49, 50] improved the radiochemical yield (RCY). The ^{89}Zr-TiO_2-Tf offers a simple integrated construct for imaging nanophotosensitizer *in vivo* and stimulating ROS for treating primary and secondary bone malignancies.

^{89}Zr-TiO_2-Tf is kinetically and thermodynamically stable

Although the radiolabeling experiments established that $^{89}Zr^{4+}$ metal ions attached to the surface of the TiO_2 NPs, this observation was not sufficient to confirm stable radiolabeling over time *in vitro* and *in vivo*. Therefore, we used ligand challenge and serum stability studies to assess the thermodynamic and kinetic stability of ^{89}Zr-TiO_2-Tf (Figure 2).[51] ^{89}Zr-TiO_2-Tf was stable in saline (Figure 2A) and 50 mM DTPA in water (Figure 2B), with > 99% of the ^{89}Zr radioactivity remaining bound to the high molecular weight NP fraction up to 72 h. In contrast, 72% of the ^{89}Zr radioactivity remained bound to TiO_2 NPs when challenged with DFO for 72 h (Figure 2C), due to its high affinity for Zr metal ions.[52] Serum challenge data (Figure 2D) demonstrated that radiolabeled NPs were stable, with <10% of the ^{89}Zr radioactivity released as low MW material from ^{89}Zr-TiO_2-Tf. These data confirmed that chelate-free, heat-induced ^{89}Zr-radiolabeling generated a thermodynamically and kinetically stable product. In all cases, the radiolabeled NPs are stable within 24 h of incubation with diverse metal chelates. Although some radioactivity was lost at 72 h using DFO, the occurrence of this high-affinity Zr chelator in rodents and humans is so low that it is not a threat for the *in vivo* use of ^{89}Zr-TiO_2-Tf.

^{89}Zr labeling does not affect the morphology of TiO_2 NPs

After demonstrating the stable radiolabeling of ^{89}Zr-TiO_2-Tf, we performed non-radioactive studies to evaluate the chemical and morphological properties of the TiO_2 NPs before and after Zr chemisorption using transmission electron microscopy (TEM) and dynamic light scattering (DLS) analysis. DLS showed that the hydrodynamic diameter of the Zr-TiO_2-Tf was comparable to the TiO_2-Tf NPs, with an average diameter of 122 nm ± 16 nm and PDI 0.14 ± 0.04 over 5 preparation experiments of the nanoparticle (Figure 3A). TEM of the Zr-TiO_2-Tf showed that Zr labeling did not affect the morphology of the TiO_2-Tf (Figure 3C), which we previously reported.[35] Coupled Plasma-Optical Emission Spectrometer (ICP-OES) analysis showed there was no detectable free Zr in the supernatant after precipitation of the nanoparticles with centrifugation, confirmed the chemisorption of >99% of Zr ions on the TiO_2 NP surfaces.

^{89}Zr-TiO_2-Tf Potentiates ROS production in cells and cell-free media

Whereas therapeutic radiopharmaceuticals can generate ionizing ROS for cell killing *via* DNA damage, diagnostic radiotracers do not produce sufficient ROS for this purpose. In the presence of appropriate photosensitizers, some radionuclides at non-therapeutic doses can stimulate ROS production to exert their cytotoxic effects.[35, 37, 53, 54] Unlike previous studies, we evaluated whether direct incorporation of a radionuclide into a nanophotosensitizer could potentiate ROS production. Using the ROS-sensor, H_2DCFDA dye to determine ROS production in a cell-free system, we found that ^{89}Zr-TiO_2-Tf generated significantly higher levels of ROS at all time points when compared to either ^{89}Zr alone or TiO_2-Tf NPs (Figure 4A). In particular, 72 h after particle formation, ^{89}Zr-TiO_2-Tf produced 30% and 60% more

ROS than TiO_2-Tf and ^{89}Zr, respectively. The apparent ROS production by TiO_2-Tf NPs could be caused by γ-emissions from neighboring wells containing ^{89}Zr.

A critical tenet of radionuclide-augmented phototherapy, also known as Cerenkov radiation induced Therapy (CRIT) is the use of sub-toxic amounts of radiopharmaceuticals and photosensitizers to induce a therapeutic response. To establish the optimal dose of each component that will not induce cytotoxicity, we treated multiple myeloma (MM1.S) cells stably transfected with click beetle red (CBR) luciferase-mCherry construct and green fluorescent protein (GFP) with increasing amount of the ^{89}Zr and determined their viability 72 h later. The data showed that radioactivity higher than 0.37 MBq significantly affected the cell viability 72 h after treatment (Figure 4B), suggesting that this amount of activity is optimal for CRIT.

Although we demonstrated that ^{89}Zr-TiO_2-Tf generates ROS in a cell-free system, eukaryotic cells have developed effective anti-oxidative pathways and mechanisms to regulate oxidative stress,[55, 56] which could prevent ^{89}Zr-TiO_2-Tf mediated ROS generation in cells. Treatment of MM cells with ^{89}Zr-TiO_2-Tf (0.37 MBq, 20 μg), followed by incubation for 72 h at 37 °C generated 25% more ROS than ^{89}Zr alone (0.37 MBq), 35% more than TiO_2-Tf (20 μg), and 38% more than the untreated cells (Figure 4C). These results demonstrate the potential use of ^{89}Zr-TiO_2-Tf for therapeutic applications.

^{89}Zr-TiO_2-Tf induces apoptosis of MM cells *in vitro*

We next evaluated the effect of ^{89}Zr-TiO_2-Tf on the viability of MM1.S cells *in vitro*. Treatment of MM1.S tumor cells with 0.37 MBq (20 μg) of ^{89}Zr-TiO_2-Tf decreased cell viability by about 50%, while neither ^{89}Zr alone nor TiO_2-Tf had any statistically significant effect (Figure 4D). The cell killing by ^{89}Zr-TiO_2-Tf could occur by multiple pathways. Apoptosis is one of the common downstream outcomes of prolonged exposure of cells to increased ROS levels.[57–59] Therefore, we evaluated the effect of ^{89}Zr-TiO_2-Tf exposure on the level of caspase-3 in MM1.S cells *in vitro*, a biomarker of caspase-mediated apoptosis. Indeed, treating MM1.S cells with 0.37 MBq (20 μg) ^{89}Zr-TiO_2-Tf for 72 h resulted in a 3.5-fold increase in activated caspase-3 compared to the untreated cells (Figure 4E). In contrast, ^{89}Zr, TiO_2-Tf, or a mixture of ^{89}Zr and TiO_2-Tf had minimal effect on caspase-3 expression. These results demonstrate that ^{89}Zr-TiO_2-Tf is capable of generating sufficient ROS to cause MM cell death, with caspase-dependent apoptosis playing a significant role.

^{89}Zr-TiO_2-Tf selectively localizes to bone marrow (BM)-containing bones

Positron emitting ^{89}Zr is an excellent radioisotope for PET imaging, allowing the imaging of ^{89}Zr-TiO_2-Tf distribution *in vivo*. To investigate the specificity of ^{89}Zr-TiO_2-Tf as an imaging agent, 1.11 MBq ^{89}Zr-TiO_2-Tf, ^{89}Zr-Tf, or ^{89}Zr-oxalate were injected intravenously (IV) into Balb/C mice (n = 5 per compound) and imaged with PET/X-rau computed tomography (CT) 48 h later. The imaging data revealed distinct localization patterns for the three compounds (Figure 5A). While ^{89} Zr-oxalate localized primarily to the spine and ^{89}Zr-Tf instead localized primarily to the liver, ^{89}Zr-TiO_2-Tf accumulated predominantly in the spine, with moderate uptake observed in the liver. Quantification of the ^{89}Zr-TiO_2-Tf images gave standard uptake values (SUV) of 42 and 10 for all bone tissue and liver, respectively

(Figure 5B). *Ex vivo* quantitative analysis of ^{89}Zr amount in excised tissue correlated with the noninvasive imaging data (Figure 5C). To confirm that ^{89}Zr-TiO_2-Tf was osteotropic and localized to the bones, we dissected the animals after the PET/CT imaging, harvested the organs, and quantified the amount of ^{89}Zr and Ti in each organ by gamma emission and ICP-OES, respectively. Both metals demonstrated excellent bone tropism, co-localizing to the bones and to a smaller extent in the liver (Figure 5D). In particular, the ^{89}Zr content in bones (42 %ID/g) was significantly higher than the amounts detected in any other organ (Figure 5C). Similarly, about 64 %ID/g of Ti was detected in the bones of animals treated with either ^{89}Zr-TiO_2-Tf or non-radiolabeled Zr-TiO_2-Tf (Figure 5D). Moreover, when the BM was separated from the matrix, it contained more than 50% of the total TiO_2 found in the bone (Figure 5E).

Similar to the previous report,[39] chelation of ^{89}Zr with DFO in ^{89}Zr-Tf decreased the bone-seeking tendency of the metal. The dual distribution of ^{89}Zr-TiO_2-Tf in the bone and liver reflects the competing Zr osteotropism and Tf-driven liver uptake. Thus, the NP functionality can be used to modulate the distribution of Zr-labeled metal NPs. Although we focused on Zr osteotropism, previous studies with ^{45}Ti-oxalate ($t_{1/2}$ = 184.8 minutes), demonstrated the accumulation of this metal in the bone tissue as early as 5 h after administration.[44, 60] This finding suggests that the chemical affinity of both Zr^{4+} and Ti^{4+} for the bone matrix could mediate or enhance the observed osteotropism. Taken together, the imaging and biodistribution results provided conclusive evidence that ^{89}Zr-TiO_2-Tf selectively localized to bone tissue, suggesting that it had the potential to provide image-guided functionality to MM CRIT.

Single-dose administration of ^{89}Zr-TiO_2-Tf inhibits MM progression *in vivo*

In addition to developing osteotropic nanophotosensitizers, we postulated that ^{89}Zr-induced ROS production could induce a therapeutic effect in a disseminated medullar MM xenograft. MM1.S cells, when administered IV in Fox Chase SCID beige mice, home to the BM and are readily detectable by a bioluminescence scanner 15–20 days later. After detecting the presence of the MM lesions in BM with bioluminescence imaging (BLI), we initiated ^{89}Zr-TiO_2-Tf therapy with a single IV injection of 1.11 MBq ^{89}Zr-TiO_2-Tf (60 μg TiO_2-Tf). We used PET/CT to monitor the distribution of the NPs (Figure 6A). As expected, the ^{89}Zr-TiO_2-Tf localized to the bones and liver and the BLI showed the engraftment of the tumors in bone tissues (Figure 6E). The tumor progression was monitored weekly with BLI. The single treatment with ^{89}Zr-TiO_2-Tf effectively suppressed tumor progression in the treated cohort compared to the untreated animals (Figure 6B). In separate experiments, we investigated whether the stable isotope of Zr-chloride, ^{89}Zr-oxalate, or ^{89}Zr-Tf would have any effect on tumor progression. These control animals received either 60 μg Zr-TiO_2-Tf (Figure 6C), 1.11 MBq (60 μg) ^{89}Zr-oxalate (Figure 6D), 1.11 MBq (60 μg) ^{89}Zr-Tf (Figure 6D), or no treatment and were monitored weekly with BLI. None of the control conditions had any appreciable effect on disease progression. These data clearly indicate that a single administration of ^{89}Zr-TiO_2-Tf resulted in specific and effective regression of MM disease progression in the treated cohort. In addition to suppressing the disease progression, animals treated with ^{89}Zr-TiO_2-Tf were still alive and presented 10-fold less tumor burden when all the untreated animals succumbed to the disease. This study demonstrates a successful application of single dose image-guided depth-independent radionuclide mediated nanophototherapy in a pre-clinical model of MM, facilitating the application of the technology in the treatment of diverse bone lesions.

Recent surge in the use of TiO_2 nanoparticles for medical applications has also raised concerns about their potential toxicity in living organisms.[61–65] Reports have shown that TiO_2 accumulates in the liver, spleen, lungs, and kidneys. The amount of organ uptake varied depending on the size and shape of the TiO_2 NPs, as well as the duration and route of particle administration. Some reports show that TiO_2 exposure induced the release of pro-inflammatory cytokines TNF-α, IL1-ß, and IL-6.[66, 67] Unlike previous reports where TiO_2 doses of 40 mg/kg and above resulted in high liver uptake and various degrees of organ dysfunction, the small dose (3 mg/kg) used in our study exhibited moderate liver uptake of Ti and low accumulation in other organs (Figure 5).

CONCLUSION

We have established a method for synthesizing bone targeting ^{89}Zr-TiO_2-Tf NPs for single-dose image-guided CRIT of MM. Chelate-free, heat-induced radiolabeling of this construct was found to be thermodynamically and kinetically stable *in vitro* through a series of ligand challenge and plasma stability tests. The ^{89}Zr-TiO_2-Tf construct showed excellent ROS generation in cell-free and MM1.S cell model. Further, PET/CT imaging and biodistribution studies of treated mice showed that ^{89}Zr-TiO_2-Tf primarily localized to the bone, with the greatest accumulation in the BM. Previous studies have shown that the BM microenvironment serves as a niche for MM cells, providing a survival advantage and resistance to current MM treatments.[68] By targeting and infiltrating this niche, we showed that our treatment suppressed MM disease progression through continuous generation of the ROS from ^{89}Zr-TiO_2-Tf NPs, proportional to the half-life of the ^{89}Zr radionuclide. Additionally, these integrated multifunctional NPs provide insight into implementing CRIT for longitudinal therapy, while also monitoring therapeutic delivery using a single therapeutic dosage. Future studies will explore the use of this approach to deliver drugs to the BM, thereby minimizing systemic and multi-organ toxicity inherent in many chemotherapeutics.

MATERIALS AND METHODS

Anatase TiO_2 nanoparticles and all other chemicals, unless otherwise stated, were purchased from Sigma Aldrich (St. Louis, MO) and were used as received. Water (>18.2 MΩ·cm at 25 °C, Milli-Q, Millipore, Billerica, MA) was purified by passing it through a 10 cm long column of Chelex resin (Bio-Rad Laboratories, Hercules, CA) at a flow rate < 1.0 mL/min, which removed common metal ion contaminants. All instruments were calibrated and maintained in accordance with manufacturers' instructions.

^{89}Zr Production and Purification

^{89}Zr was produced *via* the $^{89}Y(p,n)^{89}Zr$ reaction ay the Washington University Medical School Cyclotron Facility on a CS-15 cyclotron (Cyclotron Corporation, Berkeley, CA) and separated *via* ion exchange chromatography as previously described[69], with a resulting specific activity of 0.84–4.98MBq/μmole).

Radiochemistry

Radioactivity was measured with a Capintec CRC-15R Dose Calibrator (Capintec, Ramsey, NJ) with a calibration factor of 517 for ^{89}Zr. To accurately quantify radioactivity, experimental samples were analyzed for 1 minute on a calibrated Automatic Wizard2 Gamma Counter (Perkin Elmer, Waltham, MA), using a dynamic energy window of 800–1000 keV for ^{89}Zr (909 keV emission). Radiolabeling reactions were monitored with thin-layer chromatography (TLC) by using a radio-TLC plate reader (Lablogic, Brandon, FL). Solution pH was measured with pH paper strips (colorpHast non-bleeding strips; EMD Chemicals Inc., Gibbstown, NJ).

For labeling reactions, 10 mg/mL TiO_2 stock solution was prepared using commercial TiO_2 anatase powder suspended in metal-free water. TiO_2 NPs were radiolabeled with ^{89}Zr using heat-induced labeling without a chelator.[40] Briefly, an aqueous solution of ^{89}Zr (~ 37 MBq, approximately 0.1 mL, pH <1.0) in 1.0 M oxalic acid was transferred to a metal-free vial, and the solution was neutralized by adding 1 mL of 1.0 M 4-(2-hydroxyethyl)-1-piperazineethanesulfonic acid (HEPES) buffer, pH 7.1. To optimize the radiolabeling conditions, aliquots of 9.25 MBq of ^{89}Zr were used for each reaction, with an amount of TiO_2 ranging from 10 μg to 160 μg. Reaction tubes were incubated at 100 °C for 1 h, with mixing at 1000 RPM. The reactions were then cooled to room temperature (RT). The radiochemical purity (RCP) was measured by radio-TLC. The radiolabeled NPs were combined with 6 mg apo-Tf in a w/w ratio of 1:3 Tf to TiO_2, followed by continuous probe sonication (Cole Parmer - Ultrasonic Processor GE 130PB, Vernon Hills, IL) at 3 watts for 1 minute. The final Tf coated radiolabeled NPs were filtered through a 0.22 μm polyethersulfone (PES) syringe filter (EMD Millipore, Burlington, MA) for the subsequent experiments.

To radiolabel Tf, Tf-DFO conjugate was prepared by mixing 10 mg/mL (0.012 μmol) Tf with 0.18 μmol 1-(4-isothiocyanatophenyl)-3-[6,17-dihydroxy-7,10,18,21-tetraoxo-27-(N-acetylhydroxylamino)- 6,11,17, 22- tetraazaheptaeicosine] thiourea (*p*-SCN-Bn-DFO, Macrocyclics, Plano, TX) using 0.1 M sodium carbonate (pH 9) as the conjugation buffer. The reaction mixture was vortexed at RT for 1 h. Then *p*-SCN-Bn-DFO was conjugated to Tf *via* a thiourea linkage and the conjugate was purified using a 0.5 mL Zeba spin column with a 40 kDa molecular weight cut-off (Thermo Fisher Scientific, St Peters, MO). The protein concentration of the resultant DFO functionalized Tf was determined by bicinchoninic acid assay (Thermo Fisher Scientific, St. Peters, MO). Tf-DFO conjugate (100 μg, 1.25 nmol) was then added to neutralized ^{89}Zr-oxalate (74 MBq in 1 mL sodium carbonate buffer, pH 9), and the reaction mixture was vortexed vigorously at RT for 1 h, followed by purification using Zeba spin columns. Radiochemical purity was determined by radio-TLC, using 50 mM diethylenetriaminepentaacetic acid (DTPA) as the mobile phase. The specific activity of ^{89}Zr-Tf-DFO was 55.5 MBq/nmol.

Stability

The stability of radiolabeled TiO_2 NPs was evaluated by performing ligand challenge experiments. Radiolabeled NPs (*e.g.*, ^{89}Zr-TiO_2-Tf, 7.4 MBq, ~50 µl) were added to 450 µL solutions of either sterile saline, DFO (10 mM, pH7.0), or DTPA (50 mM, pH 7.5) and reactions were incubated at 37 °C for up to 72 h. Aliquots (15 µL) were removed at 0, 24, 48, and 72 h, and analysis of radiochemical stability was performed by using analytical size-exclusion chromatography (SEC) Sephadex G-25 (Thermo Fisher Scientific, St Peters, MO) columns, eluted with 16 × 0.5 mL fractions of solutions. Activity eluted in the first 2 mL was associated with the high molecular weight (>30 kDa) fraction, whereas activity eluted in the fractions >2.0 mL was associated with small-molecules derived from radiochemical decomposition under the ligand challenge conditions. The radiochemical stability of ^{89}Zr-TiO_2-Tf was also evaluated in normal mouse serum. Radiolabeled NPs (*e.g.* ^{89}Zr-TiO_2-Tf; 7.4 MBq; 50 µL) were incubated in either mouse or human serum (450 µL) for 72 h at 37 °C. Samples were analyzed by analytical SEC on PD-10 columns, eluted with 16 × 0.5 mL fractions of sterile saline.

Non-Radioactive Labeling Reactions

To facilitate a more detailed chemical analysis and morphology study of ^{89}Zr-labeled TiO_2 NPs, reactions were performed using non-radioactive Zr metal ion oxalate salts (^{90}Zr) evaluated for their potential to associate with TiO_2 NPs under chelate-free, heat-induced labeling conditions. Non-radioactive labeling reactions were conducted under the same conditions used in the radioactive studies with TiO_2 (0.5 mg) and Zr oxalate (0.55 mg, 2 µmol), followed by coating the labeled NP with 1.5 mg Tf. TEM and DLS were used to characterize the morphology and size of the ^{90}Zr-TiO_2-Tf NP construct. TEM was obtained using an FEI Tecnai Spirit microscope (Hillsboro, OR). The particle size distribution was measured by DLS using a Malvern Zetasizer Nano-ZS (Malvern Instruments Inc., Westborough, MA).

Reactive Oxygen Species Assay

TiO_2 NPs are known to generate ROS upon the irradiation by UV light or Cerenkov radiation. Using 0.37 MBq ^{89}Zr-TiO_2-Tf, ROS measurements were carried out in a Costar[@] 96- well black plate (Corning, NY) at RT with 2’, 7’-dichlorodihydrofluorescein diacetate (H_2DCFDA) as a ROS indicator. Measurements were performed using 0.37 MBq ^{89}Zr (same for both, ^{89}Zr-oxalate and ^{89}Zr-TiO2-Tf) and 20 µg TiO_2-Tf NPs. Emitted fluorescence was detected with a BioTeck Neo2 Hybrid Multi-Mode Reader (Winooski, VT) at 24, 48, and 72 h.

Cell Lines

MM1.S human multiple myeloma[70] cell line stably transfected with click beetle red (CBR) luciferase and green fluorescent protein (GFP) reporters was generously provided by Dr. DiPersio (Washington University School of Medicine).

In Vitro CRIT

In vitro CRIT experiments were performed in 24 well plates (TPP, Midwest Scientific, St. Louis, MO) containing 4×10^5 MM1.S human multiple myeloma cells per well in 1 mL of complete medium (CM) (Iscove's modified Dulbecco's medium), supplemented with 10% fetal bovine serum and 50 μg/mL Gentamycin. Untreated cells or cells treated with ^{89}Zr-TiO_2-Tf NPs (0.37 MBq, 20 μg, in HEPES buffer), 0.37 MBq ^{89}Zr-oxalate, or 20 μg TiO_2-Tf were added to the wells and incubated at 37°C / 5% CO_2 for 72 h. The medium was then replaced with 500 μl PBS or 100 μl RIPA lysis buffer (Cell Signaling, Danvers, MA). Cell viability was measured with CellTiter 96® Aqueous One Solution Cell Proliferation Assay (Promega, Madison, WI). Emitted fluorescence was detected with a BioTeck Neo2 Hybrid Multi-Mode Reader (Winooski, VT).

Caspase 3/7 Activity Assay

Caspase 3/7 activity were determined with Apo-ONE® Homogeneous Caspase-3/7 Assay kit (Promega, Madison, WI) according to the manufacturer's instructions. Briefly, MM1.S cells were plated in 24 well plates at 4×10^5 per well in CM followed by the treatment with ^{89}Zr-TiO_2-Tf NPs (0.37 MBq, 20 μg), 0.37 MBq ^{89}Zr-oxalate, or 20 μg TiO_2-Tf. The medium was replaced 72 h later with 250 μL PBS and 250 μL Apo-ONE® Homogeneous Caspase-3/7 reagent mixture was added to the wells and Emitted fluorescence was detected with a BioTeck Neo2 Hybrid Multi-Mode Reader (Winooski, VT).

Animal Care

All animal experiments were conducted in compliance with the Institutional Animal Care and Use Committee (IACUC) guidelines and the Guide for the Care and Use of Laboratory Animals. Fox Chase SCID beige triple-immunodeficient mice (6 weeks old) were obtained from Charles River Laboratory (Wilmington, MA). Animals were allowed to acclimatize for 1 week prior to studies, and were provided with food and water ad libitum. All compounds were suspended in 100 μL saline.

In Vivo CRIT

In vivo CRIT was performed in a disseminated xenograft model. Fox Chase SCID beige mice (n=5) were implanted with 2×10^6 of MM1.S cells in saline through the tail vein. Eight days after implantation tumor progression monitoring was initiated and repeated weekly using BLI. The flux of 10^6 photons/second was considered baseline, at which time a single dose of 1.11 MBq (60 μg) in 100 μL saline was administered.[71] The tumor burden was monitored with weekly BLI.

Bioluminescence Imaging

In vivo BLI was performed on an IVIS Lumina (PerkinElmer, Waltham, MA; Living Image 3.2, 1–300 seconds exposures, binning 2–8, FOV 12.5cm, f/stop 1, and open filter). Mice were injected intraperitoneally with 150 mg/kg D-luciferin in PBS (Gold Biotechnology, St. Louis, MO) and imaged 10 minutes later under isoflurane anesthesia (2% vaporized in O_2). The total photon flux (photons/sec) was measured from regions of interest (ROIs) over the entire ventral side of the mice, using Living Image 2.6.

Small-Animal PET/CT Imaging

Prior to imaging, mice were injected intravenously *via* the tail vein with 1.11 MBq (60 μg TiO_2-Tf) of ^{89}Zr-TiO_2-Tf suspended in 100 μl saline. At 48 h post-injection, mice (n=3) were anesthetized with 1%−2% isoflurane and imaged with an Inveon small animal PET/CT scanner (Siemens Medical Solutions, Tarrytown, NY). Static images were collected for 20 minutes and reconstructed with the maximum aposteriori probability algorithm (MAP),[72] followed by co-registration with Inveon Research Workstation (IRW) image display software (Siemens Medical Solutions, Knoxville, TN). ROIs were selected from PET images using CT anatomical guidelines, and the activity associated with them was measured with IRW software. SUV were determined as Bq/cc X animal weight/ injected dose.

In Vivo Biodistribution Studies

Biodistribution studies were conducted 168 h after ^{89}Zr-TiO_2-Tf treatment. Briefly, 1.11 MBq ^{89}Zr-TiO_2-Tf (60 μg) suspended in 100 μl saline was injected *via* the tail vein. Animals (n=4) were euthanized at selected time points after NP administration, organs of interest were harvested, weighed, and the associated radioactivity was determined with a γ-counter. After correcting for background and decay, the percent-injected dose per gram (%ID/gram) and percent-injected dose per organ (%ID/organ) were calculated by comparison to a weighed, counted standard. For non-radioactive biodistribution studies, ^{90}Zr-TiO_2-Tf (60 μg) suspended in 100 μL saline was injected in tail vein (n=4). To determine the relative amount of TiO_2 contained in the BM, the BM was removed by centrifugation at 10,000xg for 10 minutes and the TiO_2 content in BM and the remaining bone matrix was determined with induction-coupled plasma-mass spectrometry (ICP-OES).

Induction-coupled plasma-optical emission spectrometry

Mouse tissues were added to Teflon digestion vessels along with 2mL of concentrated nitric acid (70%, trace metal grade). The sealed digestion vessels were then placed into a Mars 6 Microwave Digestion System (CEM Corporation). Microwave power was ramped to reach 200°C in 20 minutes, then that temperature was maintained for 20 minutes. The sample was then cooled and diluted to 3 mL with 18MΩ DI water. A Perkin Elmer Optima 7300DV Inductively Coupled Plasma-Optical Emission Spectrometer (ICP-OES) was used to determine the Ti concentration of the diluted samples. Ti calibration standards of 1 ug/L, 10 ug/L, 100 ug/L, and 1000 ug/L were used. The internal standard (200ug/L, Sc) was continuously introduced during ICP-OES analysis. Ti concentration in the tissue was calculated by multiplying the measured Ti concentration by the dilution factor and the known sample volume then dividing by the tissue weight. Ti concentration was converted to TiO_2 concentration by multiplying by the molecular weight (M/W_{TiO2} = 79.9 g/mol) to atomic weight (M/W_{Ti} = (47.9 g/mol) ratio.

Data Analysis and Statistics

Data and statistical analyses were performed using GraphPad Prism 8.0 (GraphPad Software, Inc., La Jolla, CA) and Microsoft Excel. The data were expressed as mean ± SD, unless indicated otherwise. Differences at the 95% confidence level ($P<0.05$) were considered to be statistically significant.

ACKNOWLEDGMENT

We thank the Washington University isotope production team for routine production of ^{89}Zr and the small animal imaging facility for generating the PET/CT data. This study was supported in part by grants from the National Institutes of Health (NCI: U54 CA199092, R01 CA171651, P50 CA094056, P30 CA091842; NIBIB: R01 EB00811 and NIH Shared Instrumentation Grants S10 OD016237, S10 OD020129, S10 OD025264, and S10 OD027042).

REFERENCES

1. Cai W; Chu CC; Liu G; Wang YX, Metal-Organic Framework-Based Nanomedicine Platforms for Drug Delivery and Molecular Imaging. Small 2015, 11, 4806–4822. [PubMed: 26193176]
2. Zhou M; Melancon M; Stafford RJ; Li J; Nick AM; Tian M; Sood AK; Li C, Precision Nanomedicine Using Dual PET and MR Temperature Imaging-Guided Photothermal Therapy. J. Nucl. Med 2016, 57, 1778–1783. [PubMed: 27283932]
3. Dearling JLJ; Packard AB, Molecular Imaging in Nanomedicine - A Developmental Tool and a Clinical Necessity. J. Control. Release 2017, 261, 23–30. [PubMed: 28624600]
4. Li X; Zhang XN; Li XD; Chang J, Multimodality Imaging in Nanomedicine and Nanotheranostics. Cancer Bio. Med 2016, 13, 339–348. [PubMed: 27807501]
5. Doane TL; Burda C, The Unique Role of Nanoparticles in Nanomedicine: Imaging, Drug Delivery and Therapy. Chem. Soc. Rev 2012, 41, 2885–2911. [PubMed: 22286540]
6. Elgqvist J, Nanoparticles as Theranostic Vehicles in Experimental and Clinical Applications-Focus on Prostate and Breast Cancer. Int. J. Mol. Sci 2017, 18, 1102–1155.
7. Mosayebi J; Kiyasatfar M; Laurent S, Synthesis, Functionalization, and Design of Magnetic Nanoparticles for Theranostic Applications. Adv. Healthc. Mater 2017, 6, 1700306.
8. Zavaleta C; Ho D; Chung EJ, Theranostic Nanoparticles for Tracking and Monitoring Disease State. SLAS Technol. 2018, 23, 281–293. [PubMed: 29115174]
9. Zhang F; Zhu G; Jacobson O; Liu Y; Chen K; Yu G; Ni Q; Fan J; Yang Z; Xu F; Fu X; Wang Z; Ma Y; Niu G; Zhao X; Chen X, Transformative Nanomedicine of an Amphiphilic Camptothecin Prodrug for Long Circulation and High Tumor Uptake in Cancer Therapy. ACS Nano 2017, 11, 8838–8848. [PubMed: 28858467]
10. Huang W; Chen L; Kang L; Jin M; Sun P; Xin X; Gao Z; Bae YH, Nanomedicine-Based Combination Anticancer Therapy between Nucleic Acids and Small-Molecular Drugs. Adv. Drug Deliv. Rev 2017, 115, 82–97. [PubMed: 28624478]
11. Kemp JA; Shim MS; Heo CY; Kwon YJ, “Combo” Nanomedicine: Co-Delivery of Multi-Modal Therapeutics for Efficient, Targeted, and Safe Cancer Therapy. Adv. Drug Deliv. Rev 2016, 98, 3–18. [PubMed: 26546465]
12. Lee Y; Kim H; Kang S; Lee J; Park J; Jon S, Bilirubin Nanoparticles as a Nanomedicine for Anti-Inflammation Therapy. Angew. Chem. Int. Ed. Engl 2016, 55, 7460–7463. [PubMed: 27144463]
13. Grimm J, Cancer Nanomedicine: Therapy from Within. Nat. Nanotechnol 2015, 10, 299–300. [PubMed: 25855256]
14. Tarangelo A; Dixon SJ, Nanomedicine: An Iron Age for Cancer Therapy. Nat. Nanotechnol 2016, 11, 921–922. [PubMed: 27668797]
15. Jin Z; Wen Y; Hu Y; Chen W; Zheng X; Guo W; Wang T; Qian Z; Su BL; He Q, MRI-Guided and Ultrasound-Triggered Release of NO by Advanced Nanomedicine. Nanoscale 2017, 9, 3637–3645. [PubMed: 28247895]
16. Lok CN; Zou T; Zhang JJ; Lin IW; Che CM, Controlled-Release Systems for Metal-Based Nanomedicine: Encapsulated/Self-Assembled Nanoparticles of Anticancer Gold(Iii)/Platinum(Ii) Complexes and Antimicrobial Silver Nanoparticles. Adv. Mater 2014, 26, 5550–5557. [PubMed: 24664412]
17. Natarajan JV; Darwitan A; Barathi VA; Ang M; Htoon HM; Boey F; Tam KC; Wong TT; Venkatraman SS, Sustained Drug Release in Nanomedicine: A Long-Acting Nanocarrier-Based Formulation for Glaucoma. ACS Nano 2014, 8, 419–429. [PubMed: 24392729]

18. Zhao P; Zheng M; Luo Z; Gong P; Gao G; Sheng Z; Zheng C; Ma Y; Cai L, NIR-Driven Smart Theranostic Nanomedicine for On-Demand Drug Release and Synergistic Antitumour Therapy. Sci. Rep 2015, 5, 14258–14272. [PubMed: 26400780]
19. Kunjachan S; Gremse F; Theek B; Koczera P; Pola R; Pechar M; Etrych T; Ulbrich K; Storm G; Kiessling F; Lammers T, Noninvasive Optical Imaging of Nanomedicine Biodistribution. ACS Nano 2013, 7, 252–262. [PubMed: 23067565]
20. Amirfazli A, Nanomedicine: Magnetic Nanoparticles Hit the Target. Nat. Nanotechnol 2007, 2, 467–468. [PubMed: 18654342]
21. He L; Gu J; Lim LY; Yuan ZX; Mo J, Nanomedicine-Mediated Therapies to Target Breast Cancer Stem Cells. Front. Pharmacol 2016, 7, 313. [PubMed: 27679576]
22. Maiolo D; Del Pino P; Metrangolo P; Parak WJ; Baldelli Bombelli F, Nanomedicine Delivery: Does Protein Corona Route to the Target or Off Road? Nanomedicine (Lond) 2015, 10, 3231–3247. [PubMed: 26470748]
23. Sun Y; Kang C; Liu F; Zhou Y; Luo L; Qiao H, RGD Peptide-Based Target Drug Delivery of Doxorubicin Nanomedicine. Drug Dev. Res 2017, 78, 283–291. [PubMed: 28815721]
24. Orynbayeva Z; Sensenig R; Polyak B, Metabolic and Structural Integrity of Magnetic Nanoparticle-Loaded Primary Endothelial Cells for Targeted Cell Therapy. Nanomedicine (Lond) 2015, 10, 1555–1568. [PubMed: 26008193]
25. Kaittanis C; Nath S; Perez JM, Rapid Nanoparticle-Mediated Monitoring of Bacterial Metabolic Activity and Assessment of Antimicrobial Susceptibility in Blood with Magnetic Relaxation. PLoS One 2008, 3, e3253. [PubMed: 18810269]
26. Yung-Kang P; Lui CNP; Chen YW; Chou SW; Pi-Tai C; Yung KKL; Tsang EC, Engineered Core-Shell Magnetic Nanoparticle for MR Dual-Modal Tracking and Safe Magnetic Manipulation of Ependymal Cells in Live Rodent. Nanotechnology 2018, 29, 015102. [PubMed: 29205171]
27. Liu Z; Lammers T; Ehling J; Fokong S; Bornemann J; Kiessling F; Gatjens J, Iron Oxide Nanoparticle-Containing Microbubble Composites as Contrast Agents for MR and Ultrasound Dual-Modality Imaging. Biomaterials 2011, 32, 6155–6163. [PubMed: 21632103]
28. Schluep T; Hwang J; Hildebrandt IJ; Czernin J; Choi CH; Alabi CA; Mack BC; Davis ME, Pharmacokinetics and Tumor Dynamics of the Nanoparticle IT-101 from PET Imaging and Tumor Histological Measurements. Proc. Natl. Acad. Sci. U. S. A 2009, 106, 11394–11399. [PubMed: 19564622]
29. Polyak A; Naszalyi Nagy L; Mihaly J; Gorres S; Wittneben A; Leiter I; Bankstahl JP; Sajti L; Kellermayer M; Zrinyi M; Ross TL, Preparation and (68)Ga-Radiolabeling of Porous Zirconia Nanoparticle Platform for PET/CT-Imaging Guided Drug Delivery. J. Pharm. Biomed. Anal 2017, 137, 146–150. [PubMed: 28119212]
30. Kim SM; Chae MK; Yim MS; Jeong IH; Cho J; Lee C; Ryu EK, Hybrid PET/MR Imaging of Tumors Using an Oleanolic Acid-Conjugated Nanoparticle. Biomaterials 2013, 34, 8114–8121. [PubMed: 23932293]
31. Tromsdorf UI; Bruns OT; Salmen SC; Beisiegel U; Weller H, A Highly Effective, Nontoxic T1 MR Contrast Agent Based on Ultrasmall PEGylated Iron Oxide Nanoparticles. Nano Lett. 2009, 9, 4434–4440. [PubMed: 19799448]
32. Vidaud C; Bourgeois D; Meyer D, Bone as Target Organ for Metals: The Case of F-Elements. Chem. Res. Toxicol 2012, 25, 1161–1175. [PubMed: 22458510]
33. Goyal J; Antonarakis ES, Bone-Targeting Radiopharmaceuticals for the Treatment of Prostate Cancer with Bone Metastases. Cancer Lett. 2012, 323, 135–146. [PubMed: 22521546]
34. Jong J. M. v. D.-d.; Oprea-Lager DE; Hooft L; de Klerk JMH; Bloemendal HJ; Verheul HMW; Hoekstra OS; van den Eertwegh AJM, Radiopharmaceuticals for Palliation of Bone Pain in Patients with Castration-Resistant Prostate Cancer Metastatic to Bone: A Systematic Review. Eur. Urol 2016, 70, 416–426. [PubMed: 26391636]
35. Kotagiri N; Sudlow GP; Akers WJ; Achilefu S, Breaking the Depth Dependency of Phototherapy with Cerenkov Radiation and Low-Radiance-Responsive Nanophotosensitizers. Nat. Nanotechnol 2015, 10, 370–379. [PubMed: 25751304]

36. Tang R; Habimana-Griffin LM; Lane DD; Egbulefu C; Achilefu S, Nanophotosensitive Drugs for Light-Based Cancer Therapy: What Does the Future Hold? Nanomedicine (Lond) 2017, 12, 1101–1105. [PubMed: 28447872]

37. Kotagiri N; Cooper ML; Rettig M; Egbulefu C; Prior J; Cui G; Karmakar P; Zhou M; Yang X; Sudlow G; Marsala L; Chanswangphuwana C; Lu L; Habimana-Griffin L; Shokeen M; Xu X; Weilbaecher K; Tomasson M; Lanza G; DiPersio JF et al., Radionuclides Transform Chemotherapeutics into Phototherapeutics for Precise Treatment of Disseminated Cancer. Nat. Commun 2018, 9, 275. [PubMed: 29348537]

38. Abou DS; Thorek DL; Ramos NN; Pinkse MW; Wolterbeek HT; Carlin SD; Beattie BJ; Lewis JS, (89)Zr-Labeled Paramagnetic Octreotide-Liposomes for PET-MR Imaging of Cancer. Pharm. Res 2013, 30, 878–888. [PubMed: 23224977]

39. Holland JP; Divilov V; Bander NH; Smith-Jones PM; Larson SM; Lewis JS, ^{89}Zr-DFO-J591 for Immunopet of Prostate-Specific Membrane Antigen Expression *In Vivo*. J. Nucl. Med 2010, 51, 1293–1300. [PubMed: 20660376]

40. Boros E; Bowen AM; Josephson L; Vasdev N; Holland JP, Chelate-Free Metal Ion Binding and Heat-Induced Radiolabeling of Iron Oxide Nanoparticles. Chem. Sci 2015, 6, 225–236. [PubMed: 28553472]

41. Chen F; Ellison PA; Lewis CM; Hong H; Zhang Y; Shi S; Hernandez R; Meyerand ME; Barnhart TE; Cai W, Chelator-Free Synthesis of a Dual-Modality PET/MRI Agent. Angew. Chem. Int. Ed. Engl 2013, 52, 13319–13323. [PubMed: 24166933]

42. Goel S; Chen F; Luan S; Valdovinos HF; Shi S; Graves SA; Ai F; Barnhart TE; Theuer CP; Cai W, Engineering Intrinsically Zirconium-89 Radiolabeled Self-Destructing Mesoporous Silica Nanostructures for In Vivo Biodistribution and Tumor Targeting Studies. Adv. Sci. (Weinh) 2016, 3, 1600122. [PubMed: 27980987]

43. Ai F; Goel S; Zhan Y; Valdovinos HF; Chen F; Barnhart TE; Cai W, Intrinsically (89)Zr-Labeled Gd_2O_2S:Eu Nanophosphors with High *In Vivo* Stability for Dual-Modality Imaging. Am. J. Transl. Res 2016, 8, 5591–5600. [PubMed: 28078029]

44. Chen F; Valdovinos HF; Hernandez R; Goel S; Barnhart TE; Cai W, Intrinsic Radiolabeling of Titanium-45 Using Mesoporous Silica Nanoparticles. Acta Pharmacol. Sin 2017, 38, 907–913. [PubMed: 28414201]

45. Sun H; Li H; Weir RA; Sadler PJ, The First Specific Ti(Iv) -Protein Complex: Potential Relevance to Anticancer Activity of Titanocenes. Angew. Chem. Int. Ed. Engl 1998, 37, 1577–1579. [PubMed: 29710917]

46. Messori L; Orioli P; Banholzer V; Pais I; Zatta P, Formation of Titanium(Iv) Transferrin by Reaction of Human Serum Apotransferrin with Titanium Complexes. FEBS Lett. 1999, 442, 157–161. [PubMed: 9928993]

47. Daniels TR; Delgado T; Rodriguez JA; Helguera G; Penichet ML, The Transferrin Receptor Part I: Biology and Targeting with Cytotoxic Antibodies for the Treatment of Cancer. Clin. Immunol 2006, 121, 144–158. [PubMed: 16904380]

48. Kotagiri N; Sudlow GP; Akers WJ; Achilefu S, Breaking the Depth Dependency of Phototherapy with Cerenkov Radiation and Low-Radiance-Responsive Nanophotosensitizers. Nat. Nanotechnol 2015, 10, 370–379. [PubMed: 25751304]

49. Reddy MV; Sharma N; Adams S; Rao RP; Peterson VK; Chowdari BVR, Evaluation of Undoped and M-Doped TiO_2, Where M = Sn, Fe, Ni/Nb, Zr, V, and Mn, for Lithium-Ion Battery Applications Prepared by the Molten-Salt Method. RSC Adv. 2015, 5, 29535–29544.

50. Pan JW; Li C; Zhao YF; Liu RX; Gong YY; Niu LY; Liu XJ; Chi BQ, Electronic Properties of TiO_2 Doped with Sc, Y, La, Zr, Hf, V, Nb and Ta. Chem. Phys. Lett 2015, 628, 43–48.

51. Dilworth JR; Pascu SI, The Chemistry of PET Imaging with Zirconium-89. Chem. Soc. Rev 2018, 47, 2554–2571. [PubMed: 29557435]

52. Abou DS; Ku T; Smith-Jones PM, *In Vivo* Biodistribution and Accumulation of ^{89}Zr in Mice. Nucl. Med. Biol 2011, 38, 675–681. [PubMed: 21718943]

53. Kavadiya S; Biswas P, Design of Cerenkov Radiation-Assisted Photoactivation of TiO_2 Nanoparticles and Reactive Oxygen Species Generation for Cancer Treatment. J. Nucl. Med 2019, 60, 702–709. [PubMed: 30291195]

54. Nakamura Y; Nagaya T; Sato K; Okuyama S; Ogata F; Wong K; Adler S; Choyke PL; Kobayashi H, Cerenkov Radiation-Induced Photoimmunotherapy with (18)F-FDG. J. Nucl. Med 2017, 58, 1395–1400. [PubMed: 28408528]

55. Forrester SJ; Kikuchi DS; Hernandes MS; Xu Q; Griendling KK, Reactive Oxygen Species in Metabolic and Inflammatory Signaling. Circ. Res 2018, 122, 877–902. [PubMed: 29700084]

56. Russell EG; Cotter TG, New Insight into the Role of Reactive Oxygen Species (ROS) in Cellular Signal-Transduction Processes. Int. Rev. Cell Mol. Biol 2015, 319, 221–254. [PubMed: 26404470]

57. Sun S; Zhang C; Gao J; Qin Q; Zhang Y; Zhu H; Yang X; Yang D; Yan H, Benzoquinone Induces ROS-Dependent Mitochondria-Mediated Apoptosis in HL-60 Cells. Toxicol. Ind. Health 2018, 34, 270–281. [PubMed: 29506454]

58. Tang L; Cheng JN; Long Y; He XM; Liang GN; Tang XP; Jiang CX; Chen F, PCB 118-Induced Endothelial Cell Apoptosis Is Partially Mediated by Excessive ROS Production. Toxicol. Mech. Methods 2017, 27, 394–399. [PubMed: 28399781]

59. Du X; Shi Z; Peng Z; Zhao C; Zhang Y; Wang Z; Li X; Liu G; Li X, Acetoacetate Induces Hepatocytes Apoptosis by the ROS-Mediated MAPKs Pathway in Ketotic Cows. J. Cell. Physiol 2017, 232, 3296–3308. [PubMed: 28059455]

60. Vavere AL; Welch MJ, Preparation, Biodistribution, and Small Animal PET of ^{45}Ti-Transferrin. J. Nucl. Med 2005, 46, 683–690. [PubMed: 15809492]

61. Dhupal M; Oh JM; Tripathy DR; Kim SK; Koh SB; Park KS, Immunotoxicity of Titanium Dioxide Nanoparticles via Simultaneous Induction of Apoptosis and Multiple Toll-Like Receptors Signaling through ROS-Dependent SAPK/JNK and P38 MAPK Activation. Int. J. Nanomedicine 2018, 13, 6735–6750. [PubMed: 30425486]

62. Elgrabli D; Beaudouin R; Jbilou N; Floriani M; Pery A; Rogerieux F; Lacroix G, Biodistribution and Clearance of TiO2 Nanoparticles in Rats after Intravenous Injection. PLoS One 2015, 10, e0124490. [PubMed: 25909957]

63. He X; Reichl FX; Wang Y; Michalke B; Milz S; Yang Y; Stolper P; Lindemaier G; Graw M; Hickel R; Hogg C, Analysis of Titanium and Other Metals in Human Jawbones with Dental Implants - A Case Series Study. Dent. Mater 2016, 32, 1042–1051. [PubMed: 27298240]

64. Shakeel M; Jabeen F; Shabbir S; Asghar MS; Khan MS; Chaudhry AS, Toxicity of Nano-Titanium Dioxide (TiO_2-NP) through Various Routes of Exposure: A Review. Biol. Trace Elem. Res 2016, 172, 1–36. [PubMed: 26554951]

65. Zeman T; Loh EW; Cierny D; Sery O, Penetration, Distribution and Brain Toxicity of Titanium Nanoparticles in Rodents' Body: A Review. IET Nanobiotechnol. 2018, 12, 695–700. [PubMed: 30104440]

66. Wu T; Tang M, The Inflammatory Response to Silver and Titanium Dioxide Nanoparticles in the Central Nervous System. Nanomedicine (Lond) 2018, 13, 233–249. [PubMed: 29199887]

67. Shi H; Magaye R; Castranova V; Zhao J, Titanium Dioxide Nanoparticles: A Review of Current Toxicological Data. Part. Fibre Toxicol 2013, 10, 15. [PubMed: 23587290]

68. Basak GW; Srivastava AS; Malhotra R; Carrier E, Multiple Myeloma Bone Marrow Niche. Curr. Pharm. Biotechnol 2009, 10, 345–346. [PubMed: 19355944]

69. Holland JP; Sheh Y; Lewis JS, Standardized Methods for the Production of High Specific-Activity Zirconium-89. Nucl. Med. Biol 2009, 36, 729–739. [PubMed: 19720285]

70. Greenstein S; Krett NL; Kurosawa Y; Ma C; Chauhan D; Hideshima T; Anderson KC; Rosen ST, Characterization of the MM.1 Human Multiple Myeloma (MM) Cell Lines: A Model System to Elucidate the Characteristics, Behavior, and Signaling of Steroid-Sensitive and -Resistant MM Cells. Exp. Hematol 2003, 31, 271–282. [PubMed: 12691914]

71. Fowler JA; Mundy GR; Lwin ST; Lynch CC; Edwards CM, A Murine Model of Myeloma That Allows Genetic Manipulation of the Host Microenvironment. Dis. Model. Mech 2009, 2, 604–611. [PubMed: 19779066]

72. Qi J; Leahy RM, Resolution and Noise Properties of MAP Reconstruction for Fully 3-D PET. IEEE Trans. Med. Imaging 2000, 19, 493–506. [PubMed: 11021692]

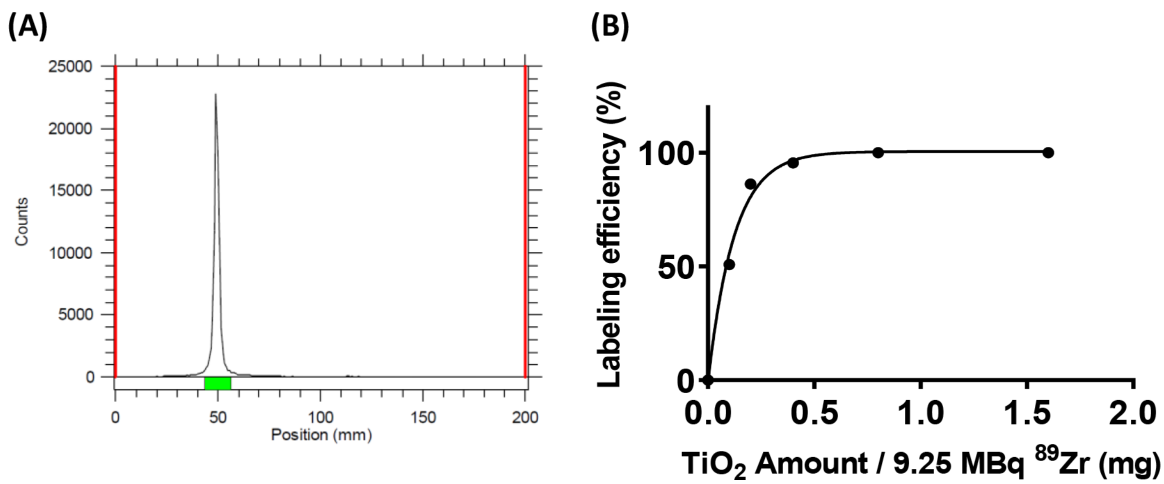

Figure 1:

Synthesis of ^{89}Zr-TiO_2-Tf (A): Radio-TLC profile of ^{89}Zr labeled TiO_2 challenged with 10 mM DTPA solution and (B): radiolabeling efficiency of ^{89}Zr-TiO_2-Tf with different amounts of TiO_2 NPs.

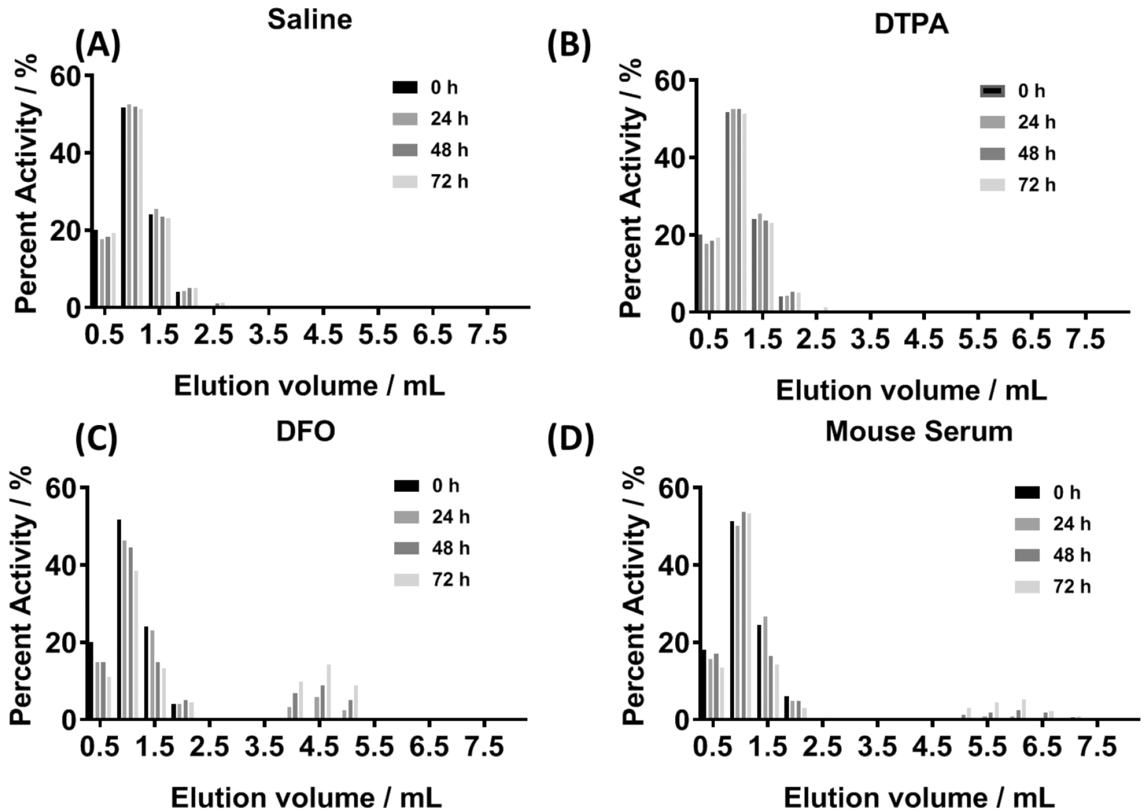

Figure 2:

Characterization of ^{89}Zr-TiO_2-Tf: Ligand challenge stability data acquired with size-exclusion chromatography at 0, 24, 48 and 72 h incubation at 37 °C in saline (A), 10 mM DTPA in water (B), 10 mM DFO in water (C), and mouse serum (D).

Author Manuscript
Author Manuscript
Author Manuscript

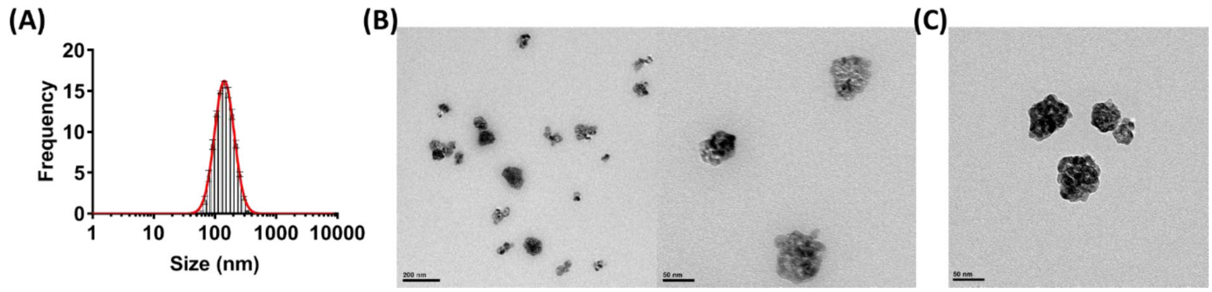

Figure 3:
Characterization of ^{89}Zr-TiO_2-Tf: (A) DLS analysis of the cold Zr labeled TiO_2-Tf NPs size distribution. (B) Representative TEM images of cold Zr labeled TiO_2-Tf NPs; (C) Representative TEM image of TiO_2-Tf NPs.

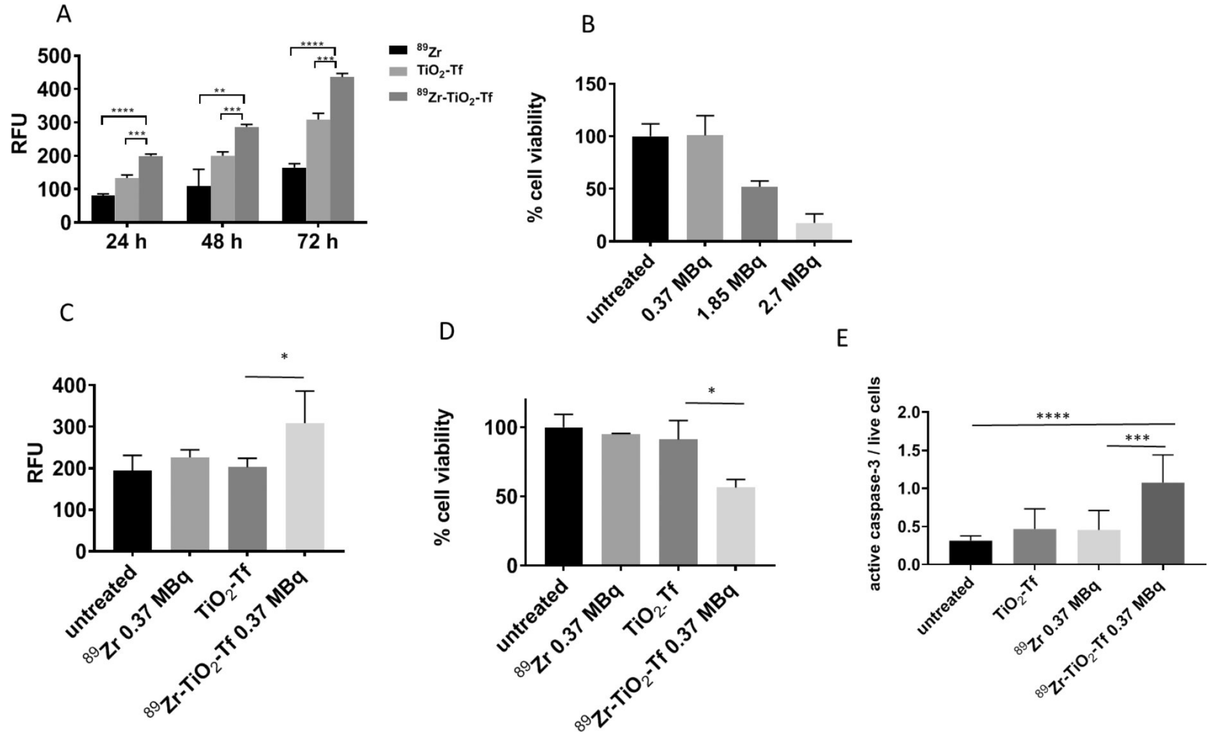

Figure 4:

In vitro properties of ^{89}Zr-TiO_2-Tf: (A) cell-free ROS production 24 h, 48 h, and 72 h after treatment with the indicated compounds; (B) MM1.S cell viability in response to different amounts of ^{89}Zr activity after treatment for 72 h; (C) ROS production by MM1.S cells 72 h after treatment with ^{89}Zr-TiO_2-Tf, ^{89}Zr, and TiO_2 compared to the untreated cells; (D) MM1.S cell viability 72 h after treatment with indicated compounds; (E) active caspase-3 levels in MM1.S cells 72 h after being treated with the indicated compounds. ^{89}Zr is used as ^{89}Zr-oxalate.

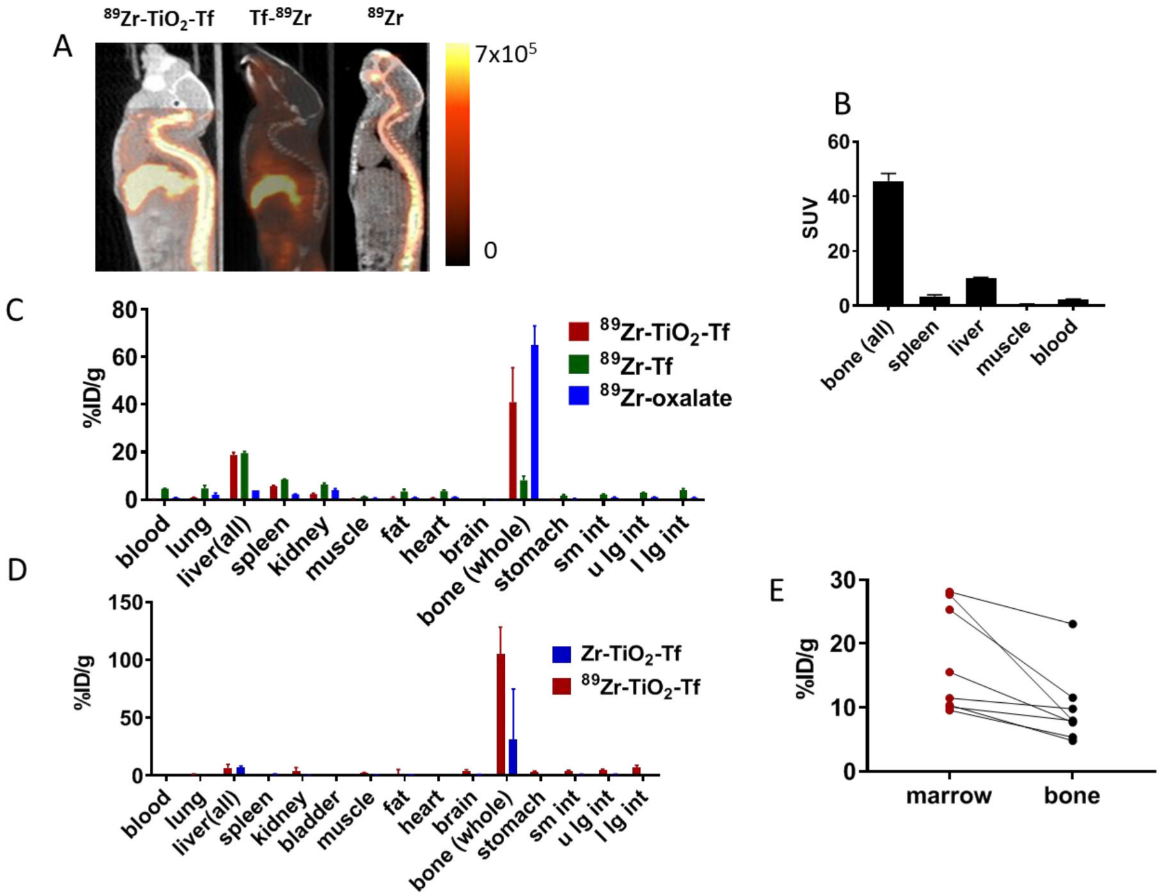

Figure 5:

In vivo properties of $^{89}Zr\text{-}TiO_2\text{-}Tf$ in Fox Chase SCID beige triple-immunodeficient mice (6 weeks old): **(A)** small animal PET/CT sagittal projections of images acquired 48 h after drug administration; **(B)** SUV for selected organs of interest obtained from images acquired 48 h after drug administration; **(C)** biodistribution of $^{89}Zr\text{-}TiO_2\text{-}Tf$, $^{89}Zr\text{-}Tf$, and ^{89}Zr-oxalate obtained with γ-emissions; **(D)** biodistribution comparison of Ti in $Zr\text{-}TiO_2\text{-}Tf$ (blue) and $^{89}Zr\text{-}TiO_2\text{-}Tf$ (red) acquired with ICP-OES 168 h after administration of compounds (60 µg of each), $p = 0.08$ for bone uptake; **(E)** TiO_2 distribution between the BM and bone matrix acquired with ICP-OES.

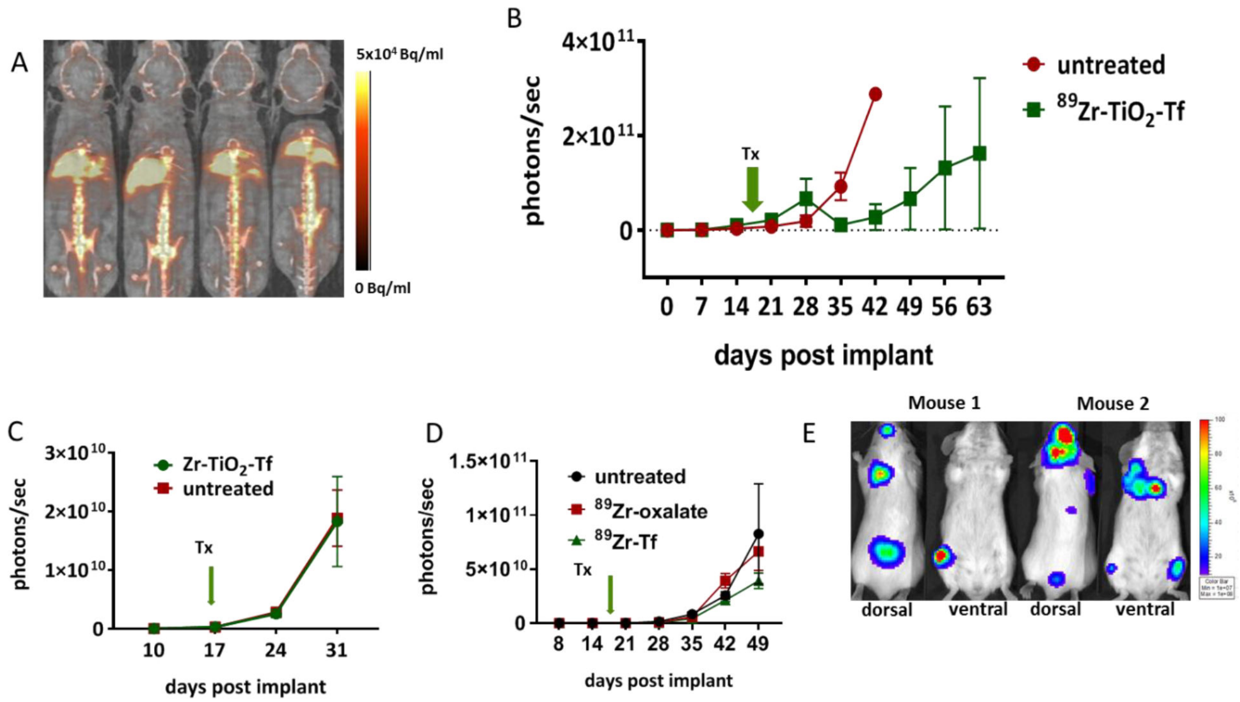

Figure 6:

Therapeutic efficacy of ^{89}Zr-TiO_2-Tf: Therapeutic study of ^{89}Zr-TiO_2-Tf (1.11 MBq/60 μg) in SCID mice bearing MM1.S: **(A)** *in vivo* drug delivery tracking by PET 48 h after administration, **(B)** rate of tumor growth (whole body photon flux) in response to ^{89}Zr-TiO_2-Tf, **(C)** rate of tumor progression (whole body photon flux) in response to treatment with Zr-TiO_2-Tf, **(D)** rate of tumor progression in response to treatment with ^{89}Zr-oxalate and ^{89}Zr-Tf, **(E)** representative BLI images showing tumor localization 50 days after implantation.

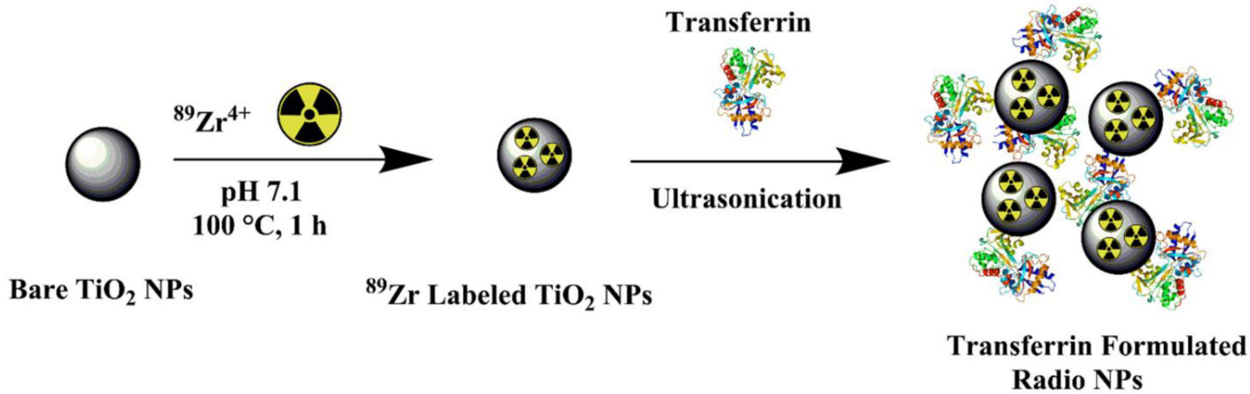

Scheme 1:
Illustration of ^{89}Zr radiolabeling of TiO_2 NP and ^{89}Zr-TiO_2-Tf formation